

See discussions, stats, and author profiles for this publication at: <https://www.researchgate.net/publication/281373236>

Detection of Zinc Finger Protein (EGR1) Based on Electrogenenerated Chemiluminescence from Singlet Oxygen Produced in a Nanoclay-Supported Porphyrin Environment

ARTICLE *in* ANALYTICAL CHEMISTRY · AUGUST 2015

Impact Factor: 5.64 · DOI: 10.1021/acs.analchem.5b01318

CITATION

1

READS

22

7 AUTHORS, INCLUDING:



Dan Shan

Nanjing University of Science and Technology

88 PUBLICATIONS 2,097 CITATIONS

SEE PROFILE

Detection of Zinc Finger Protein (EGR1) Based on Electrogenerated Chemiluminescence from Singlet Oxygen Produced in a Nanoclay-Supported Porphyrin Environment

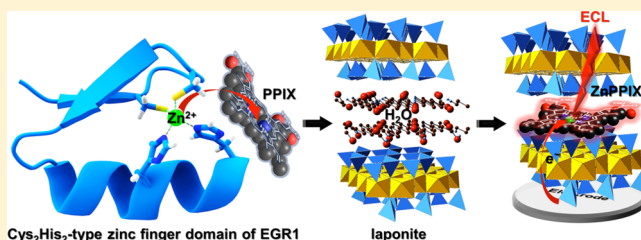
Shengyuan Deng,^{†,§} Tingting Zhang,^{†,§} Xubo Ji,[†] Ying Wan,^{†,‡} Peng Xin,[†] Dan Shan,^{*,†} and Xueji Zhang[†]

[†]Sino-French Laboratory of Biomaterials and Bioanalytical Chemistry, School of Environmental and Biological Engineering, Nanjing University of Science and Technology, Nanjing 210094, P. R. China

[‡]Intelligent Microsystem Technology and Engineering Center, School of Mechanical Engineering, Nanjing University of Science and Technology, Nanjing 210094, P. R. China

S Supporting Information

ABSTRACT: Early growth response protein 1 (EGR1), as a characteristic example of zinc finger proteins, acts as a transcription factor in eukaryotic cells, mediating protein–protein interactions. Here, a novel electrochemiluminescence (ECL)-based protocol for EGR1 assay was developed with a new eco-friendly emitter: singlet oxygen produced in the vicinity of nanoclay-supported zinc *proto*-porphyrin IX (ZnPPIX). Its electrochemical reduction stimulates an intense monochromatic CL irradiation at 644 nm from the dissolved oxygen as endogenous coreactant in the aqueous solution. This ECL derivation was rationalized via hyphenated spectroscopy and theoretical calculation. To promote hydrophilicity and solid-state immobilization of porphyrins, the lamellar artificial laponite was employed as a nanocarrier owing to its large specific area without the blackbody effect. The facile exfoliation of laponite produced quality monolayered nanosheets and facilitated the adsorption and flattening of PPIX upon the surface, resulting in a highly efficient ECL emission. Based on the release of Zn²⁺ in zinc finger domains of EGR1 upon contact with the ECL-inactive PPIX, which was monitored by circular dichroism and UV-absorption, a sensitive Zn²⁺-selective electrode for the “signal-on” detection of EGR1 was prepared with a detection limit down to 0.48 pg mL^{−1} and a linearity over 6 orders of magnitude. The proposed porphyrin-based ECL system thus infused fresh blood into the traditional ECL family, showing great promise in bioassays of structural Zn(II) proteins and zinc finger-binding nucleotides.



Early growth response protein 1 (EGR1) is a typical zinc finger protein and functions as a transcriptional regulator in mammalian cells.¹ EGR1 is able to interact with multiple proteins such as cancer biomarker p53,² and shows a distinct pattern of expression in the brain for synaptic exocytosis.³ The deficiency in EGR1 can induce downstream unsuppressed tumor in humans as well as neurogenetic diseases.^{2,4} Therefore, monitoring its level is of great significance in the research of cancer prevention and pathophysiologic mechanism.^{4,5} Conventional in vitro assessment of EGR1 employs the enzyme-linked immunosorbent assay (ELISA),^{6,7} which requires multistep processing by making use of bioengineered immunogenic antibody. Nowadays, molecular diagnoses have generally adopted digital readout platforms like spectrophotometry, electrochemistry, photoelectrochemistry, electrochemiluminescence (ECL), etc.^{8,9} Among them, the ECL technique is well-known for its synergized advantages of both electrochemistry and chemiluminescence, resulting in intrinsic high sensitivity.¹⁰ However, the primary ECL methodologies depend on the introduction of exogenous coreactant,¹¹ while environmentally incompatible nanoemitters with low ECL efficiency dominate the cathodic region.¹² Hence, it is imperative to explore green and

efficient ECL luminophores, which could simultaneously inspire new strategies for bioanalyses.

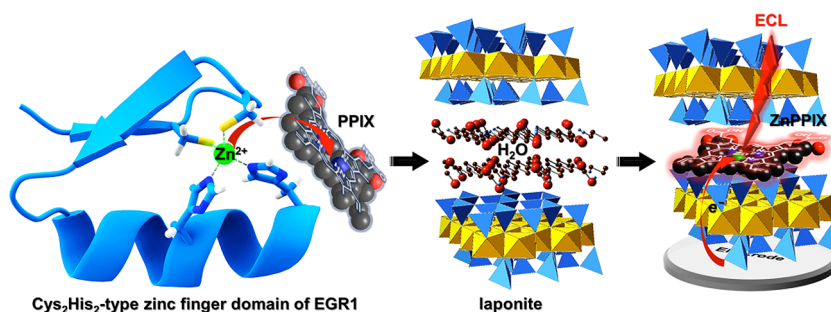
Porphyrin compounds, based on their unique molecular electronics, have been extensively applied as photovoltaic transducers, and (electro)chemical catalysts, etc.^{13,14} However, their ECL aspects have rarely been excavated so far,^{15,16} needless to say the exploit of potential applications. Here, the cathodic ECL capability of zinc *proto*-porphyrin IX (ZnPPIX) was for the first time reported, which prevailed over its homologous derivatives and other metalloporphyrins. ZnPPIX could electro-stimulate a monochromatic cathodic CL irradiation of high quantum yield at 644 nm from the endogenous dissolved oxygen, which was also chronically steady without any photobleaching. This distinctive ECL kinetics was rationalized via spectroscopic characterization and theoretical calculation.

Furthermore, in view of that EGR1 features three zinc finger (Zif) motifs where Zn²⁺ is coordinated by two-cysteine and two-histidine residues (Cys₂His₂),¹⁷ a novel method for the

Received: March 30, 2015

Accepted: August 23, 2015

Scheme 1. Schematic Illustration of Zn^{2+} -Translocation from Zif to PPIX and the Resultant ECL of ZnPPiX Supported by Laponite Nanosheets for a “Signal-On” Detection of EGRI



sensitive determination of EGRI was proposed based on the direct ECL of ZnPPiX (Scheme 1). Due to the unique stereochemistry of individual Zif for exterior binding of 5'-GCG T(G)GG GCG-3',^{18,19} the embedded multichelated zinc cations could be in situ extracted lightly by hollow PPIX. To facilitate a subsequent transfer for the solid-state ECL detection, the tissue-engineering material of laponite nanoclay was utilized as carrier owing to its large lamellar area without the blackbody effect (the ability to absorb all-spectrum radiation).^{20,21} The facile exfoliation of laponite mass-produced high-quality monolayered nanosheets with swelling hyperchannels for the intercalation of ZnPPiX.^{22,23} This eco-friendly assembly realized a stable immobilization of ZnPPiX, leading to an intense and well repeatable ECL emission. Since PPIX was contrarily unable to generate ECL, a “signal-on” ECL assay for EGRI was developed with linearity from 2 pM to 200 nM and a detection limit down to 0.48 pM (Scheme 1). The fabricated porphyrin-based system could infuse fresh new blood into the traditional ECL analyses, showing great promise in biomedical applications.

EXPERIMENTAL SECTION

Preparation of Laponite-Supported Porphyrins.

ZnPPiX as the guest was incorporated into interlayer space of the host laponite nanosheets by an intercalation protocol. The following procedures were performed for the proposed method: (1) the laponite nanosheet colloidal (2 mg mL⁻¹) was prepared by exfoliating laponite powder in the deionized water under ultrasonication for 1 h; (2) exact guest quantities of 1 mM dissolved in methanol was introduced and the mixture was stirred for 2 h to achieve a homogeneous phase, which could keep steady at room temperature for at least 3 months; (3) a defined amount of the above hybrid suspension (20 μL) was spread on the surface of GCE and dried in air. The as-prepared electrode was denoted as ZnPPiX@laponite/GCE.

As the blank control, PPIX@laponite was synthesized via the same procedure. The previously prepared PPIX@laponite/GCE was then immersed into aqueous solution containing free zinc cations or its ethylenediamine tetraacetic acid (EDTA)-chelated complexes for a given time to realize desired guest loading by the ionic exchange equilibrium. The acquired electrode surface designated as Zn^{2+} -PPIX@laponite/GCE was rinsed thoroughly with deionized water and finally dried in air at room temperature before subject to the ECL detection.

Zinc Removal and Quantification. The expression of EGRI and its reconstitution with Zn^{2+} are detailed in Supporting Information. Ten micrograms per milliliter recombinant EGRI was dialyzed against 10 mM pH 7.2 N-(2-Hydroxyethyl)piperazine-*N'*-(2-ethanesulfonic acid)

(HEPES) buffer containing 5 mM PPIX, 10 mM CaCl_2 and 100 mM NaCl at 20 $^\circ\text{C}$ for 24 h to remove Zn^{2+} . As control, apoprotein EGRI (apo-EGRI) was also formed by running EGRI on a Sephadex G-25 column (100–300 μm , 1.5 \times 30 cm, Sigma-Aldrich, Saint Louis) equilibrated with the same buffer. The overall PPIX was successively extracted from the water solution by a volume of cooled anhydrous dichloromethane (DCM) equal to that of dialysate with three solution changes. The collected ZnPPiX was then transferred in a dark vacuum drying oven for concentration.

For ECL measurement of the zinc content in EGRI, 1 mL of 2 mg mL⁻¹ laponite aqueous solution was taken as the solvent to disperse the above solid followed by the above-mentioned sensing strategy. As control, the ELISA of EGRI was also practiced, the procedures of which is in Supporting Information. For circular dichroism (CD) and UV-adsorption spectroscopies, PPIX was dissociated from EGRI by dialysis against 2 mM pH 8.0 tris(hydroxymethyl) aminomethane (Tris)-HCl, 10 mM CaCl_2 and 100 mM NaCl at 20 $^\circ\text{C}$ for another 24 h. The same solvent plus 3×10^{-5} M ZnCl_2 was used to regenerate EGRI.

Materials and Apparatus. Please see Supporting Information for the details.

RESULTS AND DISCUSSION

ECL Property of ZnPPiX. First and foremost, the ECL performance of multiple porphyrins was investigated and compared with each other. As can be seen in Figure 1A, 10 μM homogeneous ZnPPiX showed the most intense ECL emission peaking at -2.10 V with an onset of -1.68 V in the

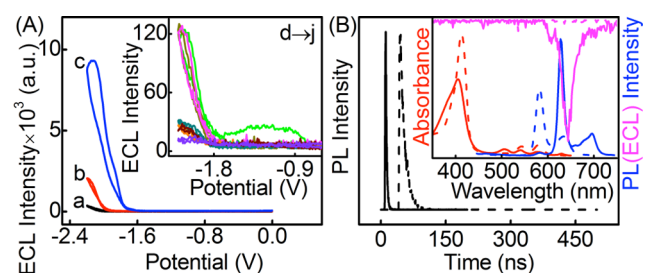


Figure 1. (A) Comparison in ECL behaviors of different porphyrins: ZnPPiX (a), ZnPcTS (b), and ZnMPiX (c) of equivalent concentration in the air-saturated detection solution. Inset of A: From d to j, ZnTMPyP, ZnPc, CuPPiX, RhPPiX, PdMPiX, FePPiX, and FeMPiX. (B) Time-resolved PL spectra of ZnPPiX (solid line) and PPIX (dashed line). Inset of B: Corresponding absorption (red), static emission (blue, excited at $(\lambda_{\text{ex}})_{\text{opt}}$), and chronoamperometric ECL (violet) spectra.

air-saturated detection solution (Figure 1A, curve c). Apart from ZnPPIX, both ZnPCtS and ZnMPIX, as its *quasi*-porphyrin complex and hydrogenated product respectively, could also generate perceptible ECL. However, their intensities appeared relatively weak only as 3.88% and 22.03% of that of ZnPPIX even at its 10-times amount (Figure 1A, curves a and b). In addition, several other metallo-porphyrins and phthalocyanine derivatives were found able to excite ECL around -2.0 V in the same condition, including ZnTMPyP, ZnPC, CuPPIX, RhPPIX, PdMPIX, FePPIX and FeMPIX (Figure 1A inset, curves d to j). All of them shared inconspicuously low luminous efficacy close to the dark noise. Therefore, a new strong ECL molecule of ZnPPIX was established. At this step, only the dissolved oxygen was assumed to serve as an endogenous coreactant. Given the saturated aqueous solubility of air under the standard atmosphere is ~ 320 μM , O_2 of less than 60 μM seems enough for ZnPPIX to energize a highly efficient ECL activity. In this way, ZnPPIX is considered to be a potent candidate available in the cathodic ECL course.

To illuminate the ECL derivation of ZnPPIX, ECL spectra were plotted to profile the hopping pathway of excitons under electrical stimulation. ZnPPIX exhibited an obvious ECL phenomenon with a full-width at half-maximum (fwhm) of 22 nm and consequently good monochromaticity at 644 nm (Figure 1B inset, violet solid); while PPIX could barely light up (Figure 1B inset, violet dashed), neither did bare GCE (data not shown). Similar to the measurement of photoluminescence (PL) quantum yield (Q.Y.), the relative ECL quantum-efficiency of ZnPPIX/ O_2 system was determined to be 0.952 , comparable with the commercialized ruthenium(II) tris(2,2'-bipyridyl) ($\text{Ru}(\text{bpy})_3^{2+}$)/*tris*-propylamine (TPrA) couple,²⁴ which prevailed over other yet rarely reported porphyrin-based anodic ECL events, such as carbonyltetrakis(3-sulfonatomesityl)porphyrin/oxalate (3.8×10^{-4}),²⁵ ruthenium(II) 2,3,7,8,12,13,17,18-octaethyl-21H,23H-porphine/TPrA (4.0×10^{-4}),¹⁶ platinum(II) octaethyl-porphyrin/TPrA (2.3×10^{-5}),²⁶ and incidentally the semiconductor nanocrystal-based ECL libraries.²⁷

Molecular spectroscopic characterizations were carried out and hyphenated to interpret the ECL spectra in the second place. As shown in Figure 1B, the optical absorption of PPIX featured an intense Soret band ($\lambda_{\text{ab}}^{\text{max}}$) at 413 nm together with a series of weak Q bands at longer wavelengths (Figure 1B inset, red dashed). In the presence of Zn^{2+} , the corresponding Soret peak was blue-shifted to 406 nm (Figure 1B inset, red solid), suggesting the electronic density of aromatic porphine ring diminished after its multidentate chelation with Zn^{2+} . This 7 nm-discrepancy in the maximal absorbance, for example, the optimal PL exciting wavelengths ($\lambda_{\text{ex}}^{\text{opt}}$), further diverged the static fluorescent properties of PPIX and ZnPPIX (vide infra).

PPIX displayed one narrow and symmetric emission peak at 586 nm with a shoulder at 638 nm (Figure 1B inset, blue dashed), which by contrast grew into the primary at 632 nm for ZnPPIX along with lesser intensities at 586 and 700 nm (Figure 1B inset, blue solid). This indicated the zinc coordination affected on both ground and excited states of porphyrin. An internal conversion must occur from Soret to Q-band after the excitation as the emission maxima partially coincided with Q bands.²⁸ The integral peak area of ZnPPIX was about twice that of PPIX, in consistence with their respective Q.Y. of 29.4% and 12.4% evaluated against Rhodamine B. In addition, the nonsplit peaks with narrow fwhm in the absorption and

the emission spectra demonstrated no apparent aggregation of porphyrin.²⁹

The analyses of time-dependent density functional theory (TD-DFT) calculations revealed qualitative agreement with experimental absorption data (Computational Details in Supporting Information). The most representative molecular frontier orbital diagrams were aligned in Figure S1 and Table S1 summarized the spin-allowed electronic transitions. The TD-DFT calculations for ZnPPIX in liquid phase of DCM reflected a strong absorption peak (Soret band) centered at 418 nm from Zn^{2+} -localized HOMO-3 and porphine-based HOMO-2 to LUMO and degenerate LUMO+1 with characteristics of intraligand charge transfer (ILCT , $b_{2u}/b_{3u} \rightarrow b_{2g}/b_{3g}$) (Figure S1, dashed lines),³⁰ which approximated ($\lambda_{\text{ab}}^{\text{max}} = 406$ nm (Figure 1B inset, violet solid). The comparatively weak broad Q-band in the visible region from 510 to 630 nm was mainly correlated to the orbital excitations from HOMO-1 and HOMO to LUMO and LUMO+1 ($a_u/b_{1u} \rightarrow b_{2g}/b_{3g}$) (Figure S1, solid lines). Given the prominent oscillation strength of HOMO-3 \rightarrow LUMO equivalent to 0.2983 , this hopping probability accordingly takes a considerable population among all ground states. The backward jump would culminate in the visible radiation around 632 nm, while the maximum emission of ECL happened at 644 nm (Figure 1B inset, violet solid). This simulation in vacuo indicated the formation of same excited state in fluorescence and ECL. Thus, the ZnPPIX-directed ECL stage could be briefed essentially as a metal-ligand charge transfer (MLCT , $d\pi_{\text{Zn}} \rightarrow \pi^*_{\text{porphine}}$).

Characterization of Laponite-Supported PPIX. To promote the aqueous solubility of PPIX and facilitate its solid-state ECL, the lamellar artificial clay of laponite was employed as matrix owing to its large specific area and optical transparency (100% transmittance for the visible light).³¹ The facile exfoliation of laponite in water produced abundant and quality chip-like nanosheets with an average lateral length of ~ 25 nm (Figure 2A and 2C). Although somehow lacking the high fidelity of an oblate shape under a less pointed tip, the selected-area height profile verified the monolayered nature of individual nanoclay with altitudes around 1.0 nm (Figure 2C lower), which drew close to the theoretical thickness (0.92 nm) of single lattice facet in bulk materials.²³ The residual flattening in *bis*-acrylic substituents of PPIX on the basal plane of laponite induced their host-guest assembly into intercalated stacks that couples of nanoaggregates emerged in the atomic force microscopic (AFM) topograph (Figure 2D).^{32,33} The sampled regional heights also grew up to ~ 1.6 nm (Figure 2D lower), suggesting the successful adsorption of monomeric PPIX on the surface of nanosheet. In addition, the chemical property of PPIX@laponite was characterized by attenuated total reflection Fourier transformation infrared (ATR-FTIR) spectroscopy (Figure 2B and Supporting Information).

Cathodic Coreactant Course of Laponite-Supported ZnPPIX. Real ECL practices always seek partnership with the coreactants, which usually turn out to be sophisticated coreactant-managed processes.³⁴ As shown in Figure 3A, ZnPPIX@laponite modified GCE could not make any cathodic ECL response in oxygen-free pH 7.4 HEPES (Figure 3A, curve a). In air-saturated buffer, the cyclic voltammogram (CV) showed a reduction peak at -0.89 V with a relatively weak shoulder at -1.35 V (Figure 3A, curve b in inset), which were assumed to be the electrochemical reduction of dissolved oxygen and its subsequent association with porphyrins, respectively;³⁵ while an intensive ECL emission with onset

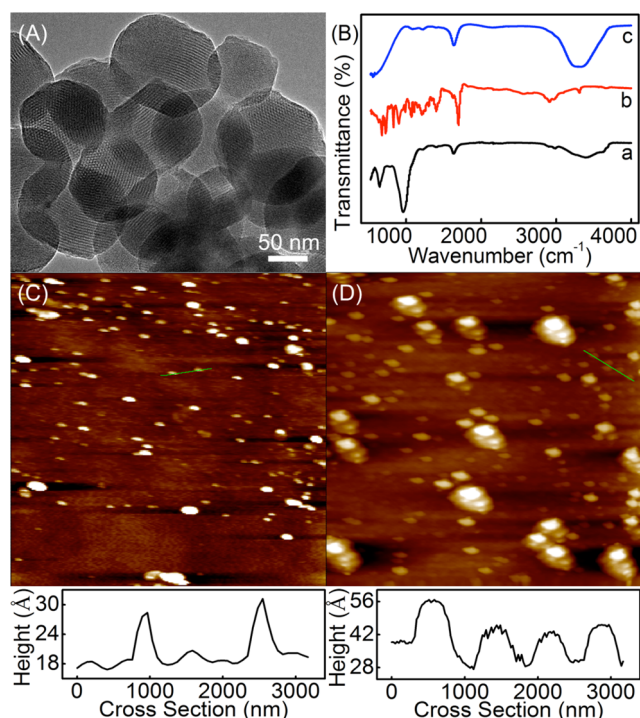


Figure 2. (A) Transmission electron micrograph of laponite nanosheets. (B) ATR-FTIR spectra of PPIX (a), laponite (b), and PPIX@laponite (c). AFM images of (C) laponite and (D) PPIX@laponite and their height profiles in the sampled area (*x*-axis indicates the total scan range).

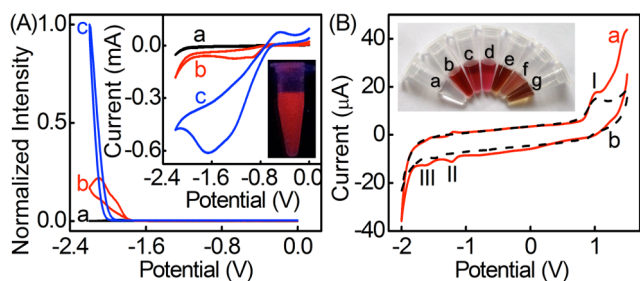
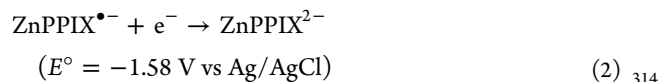
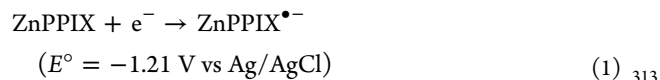
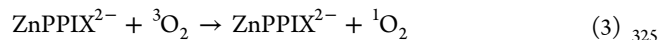


Figure 3. (A) ECL-potential curve of ZnPPiX@laponite modified GCE in the N₂-saturated (a), air-saturated (b), and O₂-saturated (c) detection solution. Inset of A: Corresponding CVs and a vial of ZnPPiX@laponite solution under UV irradiation. (B) CVs of PPIX@laponite (a) and ZnPPiX@laponite (b) in the N₂-saturated solution. Inset of B: Photographs of laponite (a), PPIX (b), Zn²⁺+PPIX (c), ZnPPiX (d), PPIX@laponite (e), Zn²⁺+PPIX@laponite (f), and ZnPPiX@laponite (g).

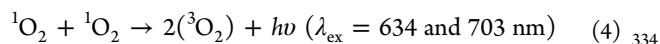
As the ECL signal is synchronously stimulated by electricity, 285 CV was further applied to investigate the intrinsic electro- 286 chemical disproportionation and annihilation in air-free dipolar aprotic solvent CH₂Cl₂. On ZnPPiX@laponite modified GCE, 288 three pairs of quasi-reversible peaks (I, II, and III) were found 289 with the formal potentials of 1.04, −1.21, and −1.58 V (vs. Ag/ 290 AgCl) (Figure 3B, curve a). The cathodic peaks corresponded 291 to ZnPPiX^{0/•−} and ZnPPiX^{•−/2−}, respectively.³⁶ These 292 reduction peak-currents (*i*_{pc}) were actually proportional to 293 the square root of scan rates from 10 to 200 mV s^{−1} (data not 294 shown), indicating that the heterogeneous electron transfer of 295 ZnPPiX@laponite followed a diffusion-controlled process. On 296 PPIX@laponite modified GCE, two redox peaks were observed 297 (Figure 3B, curve b). Peak II belonged to PPIX^{0/•−} moiety, the 298 reduction potential of which was more negative than that of 299 ZnPPiX and in accordance with the results of D'Souza et al.³³ 300 For identification of the distinguished anodic Peak III, the 301 behavior of uncoordinated PPIX was compared with that of 302 ZnPPiX. As can be seen, PPIX@laponite modified GCE 303 exhibited one peak at positive potential (PPIX^{0/+}). Therefore, 304 the wide Peak III could be ascribed to the overlap of 305 ZnPPiX^{0/+} and ZnPPiX^{•+/2+}. The potential difference of 306 2.62 V between Peak I and III was mostly consistent with 3.06 307 eV calculated from (λ_{ab})_{max} in Figure 1B inset. Their deviation 308 arose mainly from the solvation effect.³⁷ Overall, in considering 309 the energetics of this ECL system, the standard potentials of the 310 relevant half-reaction and the energy of the emitting state were 311 listed (e.g., eq 1–4): 312



As a matter of fact, there are just too many vibrational modes 315 in ZnPPiX to preclude its vibronic fine structure, which means 316 the presented monochromatic ECL and PL could only emanate 317 from a much simpler molecule in this system. In this case, the 318 ordinary paramagnetic O₂, with two unpaired electrons in its 319 frontier orbitals (termed as ³O₂ for a total spin multiplicity of 320 3), become the suspected photosource behind the images. It 321 could be that the products of eq 2 react with ³O₂ to produce 322 spin-paired singlet oxygen (¹O₂) by taking in a small amount of 323 energy from ZnPPiX^{2−} as the electron donor: 324



A more complicated mechanism might also be operative 326 where ¹O₂ is produced when the reduction product of oxygen 327 at around −1.60 V reacts with the products (or reactants) of eq 328 2, for example, ZnPPiX^{•−/2−}, since the electrode potentials are 329 very close to each other. Whatever, eq 3 continues to evolve 330 rapidly into eq 4, when ¹O₂ can react with itself to release the 331 triplet ground-state ³O₂ with red chemiluminescence that is 332 characteristic of ¹O₂.³⁸ 333



This mechanism is supported by Figure 3A, where both ECL 335 intensity and *i*_{pc} augmented with increasing O₂ concentration, 336 and would account for the increasing ECL (decreasing ratio *I*₀/*I* 337 *I*) with increasing zinc concentration (Figure 4A). The entire 338 339 implications, especially the conjecture about eq 3, need a more

272 and peak potentials of −1.77 and −2.08 V was observed under 273 a modulated photomultiplier-tube (PMT) bias of −500 V 274 (Figure 3A, curve b), implying a high ECL efficiency of 275 ZnPPiX@laponite with only the ready-made oxygen as 276 endogenous coreactant. As for the O₂-saturated solution, 277 whose concentration quintuples the partial pressure of 278 dissolved O₂ in normal air, the ECL emission enhanced 5- 279 fold correspondingly (Figure 3A, curve c) accompanied by a 280 surge of reduction current (Figure 3A, curve c in inset). The 281 significant negative-shifts in both ECL and CV peaks could be 282 justified by Nernstian equation with respect to adequate 283 coreactants, indicating otherwise that oxygen participated in the 284 rate-determining step of ECL kinetics.

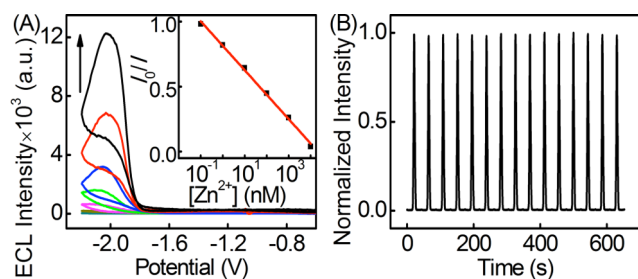


Figure 4. (A) ECL responses of PPIX@laponite to Zn²⁺ at 0.1, 1.0, 10, and 100 nM and 1.0 and 10 μM (from bottom to top) in air-saturated 10 mM pH 7.2 HEPES. Inset: Calibration curve. (B) Continuous cyclic scans of the ion-selective electrode in air-saturated 10 mM pH 7.2 HEPES after the incubation with 10 μM of Zn²⁺.

thorough clarification in future. Apparently, ZnPPIX@laponite is capable of harvesting an efficient unipolar ECL depending solely on the dissolved oxygen; while it must be concluded that this emission eventually comes from ¹O₂ dimol that is produced concomitantly during the electro-reduction of ZnPPIX.

Optimization of Parameters. Inspired by the drastic “off-on” effect on the ECL emission of porphyrin before and after the introduction of trace zinc cations shown in Figure 1A, a novel strategy for the quantification of aqueous Zn²⁺ was brought into being. Prior to such application, several experimental conditions should be optimized including the loading capacity of laponite for PPIX and the time for competitive cation-extraction by PPIX.

The uptake of PPIX into the interlayer space of the laponite was controlled in terms of a parameter named “guest-accommodation capability” defined as the amount of porphyrin vs. unit mass of laponite. Given a constant concentration of PPIX (e.g., 1.0 mM), Figure S2A provides information on the ECL intensity of PPIX@laponite composite modified GCE with diminished host loadings from 5.00 to 0.05 mg mL⁻¹ in the presence of 1 mM Zn²⁺. The maximal signal output can be obtained at 2.00 mg mL⁻¹ laponite. At its higher content, the swelling and ionic absorbability of the immobilized clay may destabilize the film-making. As a result, the modification would detach from the electrode surface under perturbation. On the other hand, the accommodating capacity for PPIX could not reach its saturation at relatively lower percentage of laponite composition, which also impacts on the ECL intensity. This optimal value of 2.00 mg mL⁻¹ coincides with that reported by Chernia et al. from both observed and calculated spectral profiles.³⁸

The time for zinc capture by PPIX during the preconcentration became another key factor. In this step, we use PL kinetic curves to real-time monitor the extraction progress from zincous molecules: typical multidentate-chelated complex and zinc finger of EGR1. The results were summarized in Figure S2B. At room temperature, upon the addition of ethylenediamine-*N,N,N',N'*-tetraacetic acid (EDTA)-coordinated Zn²⁺ (EDTA–Zn²⁺) (1.0 nM) into the cuvette of light-path-aligned PPIX solution premounted on a mini magnetic stirrer inside the dark chamber of spectrofluorometer, a maximum emission at 632 nm arose gradually as time elapsed and accessed to a plateau after 6 h (Figure S2B, curve a), demonstrating PPIX accomplished isolating Zn²⁺ from EDTA into ZnPPIX. The whole progress was also visualized with colors from crimson (PPIX, Figure 3B inset b) to magenta (ZnPPIX, Figure 3B inset d) using a hand-held UV light. The four-ligated *sp*²*d*-hybridized

Zn²⁺ in porphyrin with a formation constant (log *K*_f) of ~29.0 guaranteed higher stability than the six-ligated *sp*³*d*²-type in EDTA (log *K*_f = 16.4).³⁹ This physiochemical property of PPIX is very important for its rivalrous ligation with metallic ions in a complicated environment.

As expected, Zn²⁺ embedded within zinc fingers of EGR1 could also be removed and incorporated into PPIX, yet the entire process underwent slowly as shown in Figure S2B, curve b. ZnPPIXs have achieved this cation-exchange equilibrium beyond 9 h against 22 ng mL⁻¹ EGR1 (~1.0 nM) with a 2.8-times higher absorbance compared with curve a. This is because each EGR1 possesses three zinc fingers which have been predefined sequentially as Zif1, Zif2, and Zif3. All of them in a tetrahedral conformation of Zn(II)-binding Cys₂His₂ motif reside at C-terminal peptides with an average *K*_f value of 7.5 × 10¹² M⁻¹.⁴⁰ Thermodynamically, the tight solvent-accessible Van de Waals surface of α-helix surrounding each zinc finger would be breached; then zinc fingers of EGR1 unfold in the *apo*-state to release Zn(II) cofactors irreversibly upon contact with PPIX, fulfilling a thorough scavenging of Zn²⁺ contents. The snapshots also illustrate these phase changes from reddish brown (Figure 3B inset e) to brownish yellow (Figure 3B inset g). Hence, 9 h was chosen as an appropriate time for the reaction between PPIX and EGR1.

Quantifiability of Zn²⁺ and ECL Specificity Study. According to the “signal-on” effect on the cathodic ECL emission of PPIX@laponite, a facile analytical strategy for the detection of aqueous Zn²⁺ was proposed. Under the optimum conditions, the emission of the developed sensor intensified progressively with the increasing concentration of EDTA–Zn²⁺ in the detection solution. This growth pattern follows the Stern–Volmer equation:

$$I_0/I = 1 + K_{sv} \times c[Q] \quad (4)$$

where *I*₀ and *I* are the initial intensity and the intensity at a certain concentration of “quencher” *c*[*Q*], respectively; and *K*_{sv} as the slope is the Stern–Volmer coefficient (Figure 4A), indicating the rate-determining step obeys the static quenching rule derived from Poisson statistic model. The calibration plot showed a fairly good linearity of the reciprocal of intensity and the concentration of analyte in a range from 0.1 nM to 10 μM (*R*² = 0.997) with a detection limit of 57 pM at a signal-to-noise ratio of 3 (Figure 4A inset). For free zinc ions, given the solubility-product constant (*K*_{sp}) of Zn(OH)₂ is 3.0 × 10⁻¹⁷, while –log *K*_f of Zn(OH)₄²⁻ is 14.5 (25 °C),³⁹ no deposition predicts to turn up within this range. *K*_{sv} was calculated to be 2.1 × 10⁷ M⁻¹, indicating a very sensitive response of PPIX@laponite modified GCE to the analyte. This mainly owes to the smectic hyperchannels of hectorite-like laponite,^{23,32} which facilitated the cationic permeation and exchange with internal protons and in consequence promoted the ECL performance. In addition, 15 measurements of ECL emission upon continuous cyclic scans of the ECL sensor at 10 μM Zn²⁺ showed coincident signal with RSD of 0.12% (Figure 4B). Moreover, the ECL emission was quite stable in the next hundreds of circulations, demonstrating excellent reliability and stability of the detection signal.

To evaluate the selectivity of our proposed sensing system, the influences of common 17 cations and 14 anions including the blank solution on the ECL intensity were examined. As shown in Figure S3, neither any cation (Figure S3A) nor any anion (Figure S3B) candidate was capable of triggering observable ECL at PPIX@laponite modified GCE even at a 448

rather high concentration of 1.0 mM except for trace amount of Zn^{2+} (10.0 nM), suggesting excellent *anti*-interfering ability and specificity toward Zn^{2+} screening. Among all the coexisting ions, several metallic ions such as Mg^{2+} , Co^{2+} , Cu^{2+} , Sn^{2+} , Al^{3+} , and Fe^{3+} could take the same multidentate interaction with PPIX as Zn^{2+} does, which means that they may simultaneously occupy portions of finite ECL-active sites of porphyrins. However, this circumstance only happens at physiologically untolerated concentrations, thus would not deprive Zn^{2+} of its function as ECL origination. In practice, the fluctuation on the Zn PPIX-based ECL as a result of coreactant consumption via electrocatalysis by Co^{II} - or Fe^{III} -PPIX was negligible, because the dissolved oxygen replenished soon enough during the cyclic scans. At last, a simple ECL-based Zn^{2+} -selective electrode was constructed and ready for the succedent zinc proteinate assay.

Kinetic Insight into Zinc Extraction. The metal-induced protein folding event of recombinant as holoprotein (*holo*-), *apo*-, and zinc-regenerated EGR1 was monitored and verified by circular dichroism (CD) and UV-vis spectra. In Figure 5A

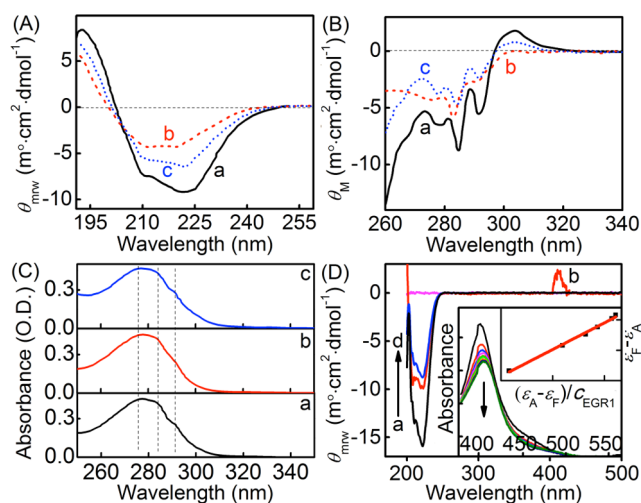


Figure 5. CD spectra of *holo*- (a), *apo*- (b), and zinc-regenerated (c) EGR1 in the (A) peptide and (B) aromatic region. (C) UV spectra of *holo*- (a), *apo*- (b), and zinc-regenerated (c) EGR1. (D) CD spectra of *holo*-EGR1 (a), *holo*-EGR1+PPIX (b), *apo*-EGR1+PPIX (c), and PPIX (d). Inset: UV spectra of the mixtures of 5.0 nM PPIX and 0, 1.4, 2.7, 5.4, 10.7, and 21.4 ng mL⁻¹ EGR1 (from top to bottom) in 10 mM pH 7.2 HEPES and plot of $(\epsilon_F - \epsilon_A)$ vs $(\epsilon_A - \epsilon_F)/[\text{EGR1}]$.

and 5B, the CD spectra of peptide and aromatic regions are expressed in terms of mean residue weight ellipticity (θ_{mrw}) and molar ellipticity (θ_M), respectively. For *holo*-EGR1, there are two minima ($\theta_{\text{mrw}} = -7.409$ and -9.178) at 210.4 and 221.4 nm and a maximum ($\theta_{\text{mrw}} = 8.367$) at 192.3 nm (Figure 5A, curve a). Using an empirical equation: $\theta_{221} = -30.3f_H - 2.34$,^{41,42} substantial amounts of α -helical formation ($\sim 22\%$) could be solved out. Assuming f_H to be 0.23,⁴¹ f_β and f_R were estimated using the formulas

$$\theta_{\text{mrw}} = f_\alpha \cdot x_\alpha + f_\beta \cdot x_\beta + f_C \cdot x_C \quad (5)$$

$$f_\alpha + f_\beta + f_C = 1 \quad (6)$$

where f_α , f_β , and f_R referred to the fraction of α -helix, β -sheet, and random-coil conformation, respectively, and x values also calculated.⁴³ θ_{mrw} at 192.3, 221.4, 231.1, and 240.6 nm were plugged in the calculations. Estimates of 8% β -structure and 70% random-coil were thus obtained for *holo*-EGR1. For *apo*-

EGR1, minima lie at 211.4 and 219.7 nm both with $\theta_{\text{mrw}} = 484 \sim 4.300$ (Figure 5A, curve b), that is, a 6% α -helix content. It was not possible to have enough wavelengths to determine the maximum for *apo*-EGR1.⁴¹ The regenerated EGR1 had a CD spectrum in the midway between the other two, containing $\sim 16\%$ α -helix ($\theta_{\text{mrw}} = -6.419$, 221.8 nm) (Figure 5A, curve c).

Similarly, the CD spectra in the aromatic region suggest structural changed with the removal of zinc (Figure 5B).⁴¹ For recombinant EGR1 (Figure 5B, curve c), a positive peak at 304.0 nm is probably due to disulfides; and tryptophan was likely responsible for the negative 284.8 and 291.2 nm peaks, while the 279.0 and 284.8 nm ones may be attributed to either tryptophan and tyrosine respectively, or both.^{41,44} A shoulder at 268.1 nm is a possible indication of the presence of phenylalanine.^{41,44}

The UV spectrum of *holo*-EGR1 shown in Figure 5C, curve a, has single peak (277.4 nm) and double shoulders (283.6 and 291.5 nm), roughly corresponding to negative peaks of its CD spectrum. The shoulders became much less pronounced as the isolation of zinc (Figure 5C, curve b). This change in the absorbance was accompanied by a similar variation in Figure 5B, curve b, of a notable decrease in the spectral fine structure and an apparent blue shift. On the other hand, the spectra of zinc finger protein are different markedly. The positive 304.0 nm peak disappeared; while a negative 291.0 nm shoulder came into being, along with negative peaks at 283.0 and 275.6 nm. Likewise for zinc-regenerated protein (curve c in Figure 5B and 5C), both fine structure and shoulders of EGR1 reappear at identical wavelengths yet at lower intensities. Thus, zincous removal caused large structural disturbances.

The formation of PPIX-Zif-EGR1 complex as a *meta*-stable state during the zinc transition was also screenshotted by CD and UV-vis spectra. Neither protein nor free PPIX showed any detectable CD band beyond 400 nm (Figure 5D, curves a and d), while a new positive-induced absorption peak occurred at 410.5 nm after mixing PPIX with *holo*-EGR1 solution (Figure 5D, curve b). This appearance has been considered to be the existence of a distorted tetrahedral structure in some Zn^{2+} -enzyme complexes.⁴⁰ This situation is in stark contrast to the case of PPIX and *apo*-EGR1 (Figure 5D, curve c), indicating the temporary association between PPIX and *holo*-EGR1 to form PPIX-Zif-EGR1 complex. The UV-vis spectrum of PPIX shows the typical Soret absorption band at 413.3 nm. With the increasing concentration of zinc finger proteins in PPIX solution, the peak intensity increased and the peak slightly shifted toward 410 nm (Figure 5D inset), the same wavelength as the CD absorption peak of PPIX-Zif-EGR1 (Figure 5D, curve b), further validating this replacement reaction of Zn^{2+} from the donor EGR1 to the acceptor PPIX. The hypochromicity and the positive-induced CD band in the visible region indicated the transient binding of PPIX to zinc fingers of EGR1. The binding constant, K , could be determined with the following equation:^{45,46}

$$\epsilon_F - \epsilon_A = (\epsilon_B - \epsilon_F)/([\text{EGR1}] \cdot K) + \Delta\epsilon \quad (7)$$

where ϵ_A is the absorbance of a given solution divided by the total PPIX concentration, ϵ_F and ϵ_B are molar absorptivities of free and bound PPIX, respectively, and $\Delta\epsilon = \epsilon_B - \epsilon_F$.⁴⁵ From the Figure 5D inset, the K and ϵ_B values were obtained to be $1.6 \times 10^4 \text{ M}^{-1}$ and $1.7 \times 10^3 \text{ M}^{-1} \text{ cm}^{-1}$, respectively, indicating a high Zif-philicity of PPIX to EGR1.

ECL Detection of EGR1 and Analytical Performance. Under the optimum conditions, the ECL intensity of the

developed protein assay enhanced with the increasing concentration of EGR1 by zincous extraction (Figure 6A).

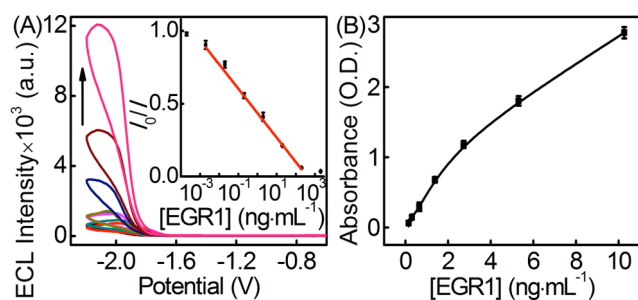


Figure 6. (A) ECL responses of PPIX@laponite to EGR1 at 1.0, 2.0, 20, and 200 pg mL⁻¹ and 2.0, 20, and 200 ng mL⁻¹ (from bottom to top). Inset: Corresponding calibration curve. (B) Calibration curve of EGR1 following a standard ELISA protocol.

The calibration plot showed a good linear relationship between the reciprocal of ECL intensity and the logarithm value of EGR1 concentration in a detection range from 2 pg mL⁻¹ to 200 ng mL⁻¹ with a correlation coefficient (R^2) of 0.991 (Figure 6A inset). The detection limit at a signal-to-noise ratio of 3 ($n = 3$) was 0.48 pg mL⁻¹, which was at least 100 times lower than the result from the commercialized ELISA (61 pg mL⁻¹) as a control (Figure 6B). More importantly, this non-immunological protein analysis showed a broadening linearity over 5 orders of magnitude and avoided the need of deoxygenating for electrochemical immunoassay.

Reproducibility, Precision, and Application of Protein Assay. The intra-assay and interassay precisions of the ECL sensor were examined by detecting 0.1 ng mL⁻¹ EGR1. The relative standard deviation (RSD) for five measurements with the same non-immunosensor was 3.1%, while the RSD for five parallel measurements with five separate electrodes was 8.0%, indicating good precision and acceptable fabrication reproducibility. Ten measurements of ECL emission at 0.1 ng mL⁻¹ EGR1 upon continuous cyclic scans showed coincident signal with RSD of 0.27%, suggesting excellent reliability and stability of the detection signal. The application potential of the developed strategy was evaluated by comparing the assay results with the references obtained by ELISA. According to the standard protocol detailed in the section of “ELISA of EGR1”, a fit curve was first drawn by plotting assayed optical density value vs. analyte concentration (Figure 6B). The results demonstrated good accuracy of the proposed method for the determination of EGR1 (Table S2).

CONCLUSIONS

This work demonstrated a new strategy for EGR1 assay based on the extraction of zinc cation from its zinc finger domains by hollow PPIX and subsequent ECL signal transduction via the formed ZnPPiX@laponite. It is found that the electro-reduction of ZnPPiX induced a highly intense and well monochromic CL emission from the dissolved O₂ as an endogenous coreactant. Hyphenated spectrometries and molecular simulation validated the intramolecular electronics of ZnPPiX-derived ECL as metal–ligand charge transfer, while CV associated with the time-resolved fluorescence illuminated this coreactant-energized ECL S-route. For practical application, laponite nanosheets were utilized to manage the assembly and immobilization of PPIX, resulting in a novel green ECL

nanocomposite. With the optimization of parameters, a sensitive ECL-based Zn²⁺-selective electrode has been devised for the zinc finger protein assay in a “turn-on” mode. Using EGR1 as a typical model, its protein folding as a result of zinc removal by PPIX was verified by CD and UV spectra. This porphyrin-based protocol could detect EGR1 down to sub-picogram level with excellent precision and reproducibility. Therefore, zinc porphyrins, as a class of potent candidates, could greatly expand the available and economic emitters of ECL technology. Meanwhile, in view of the biomedical significance of zinc finger-bound nucleic acids, the strategic paradigm in this work could be adapted to determine these special sequences, bolstering brand-new approaches for ECL-based biosensing and bioanalysis.

ASSOCIATED CONTENT

Supporting Information

The Supporting Information is available free of charge on the ACS Publications website at DOI: 10.1021/acs.analchem.5b01318.

Materials and reagents, apparatus, computational details, expression of EGR1, ELISA of EGR1, time-resolved PL spectroscopy of ZnPPiX, ATR-FTIR spectroscopy of laponite-supported PPIX, energy diagram of selected spin-allowed molecular orbitals and graphical representation for frontier molecular orbitals of ZnPPiX in DCM, effect of the concentration of laponite on the ECL intensity, PL kinetic plot, normalized ECL intensities, main experimental and calculated optical transitions of ZnPPiX, and assay results of clinical serum samples using the proposed and reference methods (PDF)

AUTHOR INFORMATION

Corresponding Author

*Phone/Fax: +86–25–84303107. E-mail: danshan@njust.edu.cn.

Author Contributions

*S.D. and T.Z. contributed equally.

Notes

The authors declare no competing financial interest.

ACKNOWLEDGMENTS

This research was supported by National Natural Science Foundation of China (Grant No. 21105048, 21175114, 21305067, 61371039), Natural Science Foundation of Jiangsu Province (BK20130754), PhD Fund of MOE for Young Teachers (0133219120019), the Fundamental Research Funds for the Central Universities (30920140112009, 30915015101), and State Key Laboratory of Analytical Chemistry for Life science (SKLACLS1302).

REFERENCES

- (1) Mali, P.; Yang, L. H.; Esvelt, K. M.; Aach, J.; Guell, M.; DiCarlo, J. E.; Norville, J. E.; Church, G. M. *Science* **2013**, 339, 823–826.
- (2) Liu, X. G.; Zhang, P.; Bao, Y.; Han, Y. M.; Wang, Y.; Zhang, Q.; Zhan, Z. Z.; Meng, J.; Li, Y. K.; Li, N.; et al. *Proc. Natl. Acad. Sci. U. S. A.* **2013**, 110, 11097–11102.
- (3) Wang, H. Y.; Yang, H.; Shivalila, C. S.; Dawlaty, M. M.; Cheng, A. W.; Zhang, F.; Jaenisch, R. *Cell* **2013**, 153, 910–918.
- (4) Enders, A.; Short, A.; Miosge, L. A.; Bergmann, H.; Sontani, Y.; Bertram, E. M.; Whittle, B.; Balakrishnan, B.; Yoshida, K.; Sjollem, G.; et al. *Proc. Natl. Acad. Sci. U. S. A.* **2014**, 111, 4513–4518.

- (5) Lee, H.; Komano, J.; Saitoh, Y.; Yamaoka, S.; Kozaki, T.; Misawa, T.; Takahama, M.; Satoh, T.; Takeuchi, O.; Yamamoto, N.; Matsuura, Y.; Saitoh, T.; Akira, S. *Proc. Natl. Acad. Sci. U. S. A.* **2013**, *110*, 12379–12384.
- (6) Gersbach, C. A.; Gaj, T.; Barbas, C. F. *Acc. Chem. Res.* **2014**, *47*, 2309–2318.
- (7) Kettleborough, R. N. W.; Busch-Nentwich, E. M.; Harvey, S. A.; Dooley, C. M.; de Bruijn, E.; van Eeden, F.; Sealy, I.; White, R. J.; Herd, C.; Nijman, I. J.; Fenyes, F.; Mehroke, S.; Scahill, C.; Gibbons, R.; Wali, N.; Carruthers, S.; Hall, A.; Yen, J.; Cuppen, E.; Stemple, D. L. *Nature* **2013**, *496*, 494–497.
- (8) Fosdick, S. E.; Knust, K. N.; Scida, K.; Crooks, R. M. *Angew. Chem., Int. Ed.* **2013**, *52*, 10438–10456.
- (9) Zhao, W. W.; Xu, J. J.; Chen, H. Y. *Chem. Rev.* **2014**, *114*, 7421–7441.
- (10) Xu, J. J.; Zhao, W. W.; Song, S. P.; Fan, C. H.; Chen, H. Y. *Chem. Soc. Rev.* **2014**, *43*, 1601–1611.
- (11) Nepomnyashchii, A. B.; Bard, A. J. *Acc. Chem. Res.* **2012**, *45*, 1844–1853.
- (12) Li, L. L.; Wu, G. H.; Yang, G. H.; Peng, J.; Zhao, J. W.; Zhu, J. J. *Nanoscale* **2013**, *5*, 4015–4039.
- (13) Mathew, S.; Yella, A.; Gao, P.; Humphry-Baker, R.; Curchod, B. F. E.; Ashari-Astani, N.; Tavernelli, I.; Rothlisberger, U.; Nazeeruddin, M. K.; Gratzel, M. *Nat. Chem.* **2014**, *6*, 242–247.
- (14) Cao, R. G.; Thapa, R.; Kim, H.; Xu, X. D.; Kim, M. G.; Li, Q.; Park, N.; Liu, M. L.; Cho, J. *Nat. Commun.* **2013**, DOI: 10.1038/ncomms3076.
- (15) Sooambar, C.; Troiani, V.; Bruno, C.; Marcaccio, M.; Paolucci, F.; Listorti, A.; Belbakra, A.; Armaroli, N.; Magistrato, A.; De Zorzi, R.; Geremia, S.; Bonifazi, D. *Org. Biomol. Chem.* **2009**, *7*, 2402–2413.
- (16) Bolin, A.; Richter, M. M. *Inorg. Chim. Acta* **2009**, *362*, 1974–1976.
- (17) Fu, Y. F.; Sander, J. D.; Reyon, D.; Cascio, V. M.; Joung, J. K. *Nat. Biotechnol.* **2014**, *32*, 279–284.
- (18) Persikov, A. V.; Singh, M. *Nucleic Acids Res.* **2014**, *42*, 97–108.
- (19) Joung, J. K.; Sander, J. D. *Nat. Rev. Mol. Cell Biol.* **2013**, *14*, 49–55.
- (20) Gaharwar, A. K.; Mihaila, S. M.; Swami, A.; Patel, A.; Sant, S.; Reis, R. L.; Marques, A. P.; Gomes, M. E.; Khademhosseini, A. *Adv. Mater.* **2013**, *25*, 3329–3336.
- (21) Li, H. R.; Li, M.; Wang, Y.; Zhang, W. J. *Chem.—Eur. J.* **2014**, *20*, 10392–10396.
- (22) He, Y. Q.; Wu, F.; Sun, X. Y.; Li, R. Q.; Guo, Y. Q.; Li, C. B.; Zhang, L.; Xing, F. B.; Wang, W.; Gao, J. P. *ACS Appl. Mater. Interfaces* **2013**, *5*, 4843–4855.
- (23) Wang, G. Y.; Maciel, D.; Wu, Y. L.; Rodrigues, J.; Shi, X. Y.; Yuan, Y.; Liu, C. S.; Tomas, H.; Li, Y. L. *ACS Appl. Mater. Interfaces* **2014**, *6*, 16687–16695.
- (24) Sentic, M.; Milutinovic, M.; Kanoufi, F.; Manojlovic, D.; Arbault, S.; Sojic, N. *Chem. Sci.* **2014**, *5*, 2568–2572.
- (25) Chen, F. C.; Ho, J. H.; Chen, C. Y.; Su, Y. O.; Ho, T. I. *J. Electroanal. Chem.* **2001**, *499*, 17–23.
- (26) Long, T. R.; Richter, M. M. *Inorg. Chim. Acta* **2005**, *358*, 2141–2145.
- (27) Tan, J.; Xu, L. R.; Li, T.; Su, B.; Wu, J. M. *Angew. Chem., Int. Ed.* **2014**, *53*, 9822–9826.
- (28) Bentley, K. W.; Wolf, C. J. *Am. Chem. Soc.* **2013**, *135*, 12200–12203.
- (29) Xue, T.; Jiang, S.; Qu, Y. Q.; Su, Q.; Cheng, R.; Dubin, S.; Chiu, C. Y.; Kaner, R.; Huang, Y.; Duan, X. F. *Angew. Chem., Int. Ed.* **2012**, *51*, 3822–3825.
- (30) den Boer, D.; Li, M.; Habets, T.; Iavicoli, P.; Rowan, A. E.; Nolte, R. J. M.; Speller, S.; Amabilino, D. B.; De Feyter, S.; Elemans, J. A. A. W. *Nat. Chem.* **2013**, *5*, 621–627.
- (31) Angelini, R.; Zaccarelli, E.; Marques, F. A. M.; Sztucki, M.; Fluerașu, A.; Ruocco, G.; Ruzicka, B. *Nat. Commun.* **2014**, DOI: 10.1038/ncomms5049.
- (32) Nakato, T.; Ueda, H.; Hashimoto, S.; Terao, R.; Kameyama, M.; Mouri, E. *ACS Appl. Mater. Interfaces* **2012**, *4*, 4338–4347.
- (33) Bujdak, J.; Chorvat, D.; Iyi, N. *J. Phys. Chem. C* **2010**, *114*, 1246–1252.
- (34) Wu, P.; Hou, X. D.; Xu, J. J.; Chen, H. Y. *Chem. Rev.* **2014**, *114*, 11027–11059.
- (35) Lazarides, T.; Sazanovich, I. V.; Simaan, A. J.; Kafentzi, M. C.; Delor, M.; Mekmouche, Y.; Faure, B.; Reglier, M.; Weinstein, J. A.; Coutsolelos, A. G.; Tron, T. J. *Am. Chem. Soc.* **2013**, *135*, 3095–3103.
- (36) Wu, H.; Fan, S. H.; Jin, X. Y.; Zhang, H.; Chen, H.; Dai, Z.; Zou, X. Y. *Anal. Chem.* **2014**, *86*, 6285–6290.
- (37) D'Souza, F.; Amin, A. N.; El-Khouly, M. E.; Subbaiyan, N. K.; Zandler, M. E.; Fukuzumi, S. *J. Am. Chem. Soc.* **2012**, *134*, 654–664.
- (38) Di Mascio, P.; Sies, H. *J. Am. Chem. Soc.* **1989**, *111*, 2909–2914.
- (39) Chernia, Z.; Gill, D. *Langmuir* **1999**, *15*, 1625–1633.
- (40) Lide, D. R. *CRC Handbook of Chemistry and Physics*, 88th ed.; CRC Press Inc.: Boca Raton, FL, 2008.
- (41) Bjarnason, J. B.; Tu, A. T. *Biochemistry* **1978**, *17*, 3395–3404.
- (42) Chan, K. L.; Bakman, I.; Marts, A. R.; Batir, Y.; Dowd, T. L.; Tierney, D. L.; Gibney, B. R. *Inorg. Chem.* **2014**, *53*, 6309–6320.
- (43) Fiedler, S.; Cole, L.; Keller, S. *Anal. Chem.* **2013**, *85*, 1868–1872.
- (44) Mendonca, L.; Hache, F.; Changenet-Barret, P.; Plaza, P.; Chosrowjan, H.; Taniguchi, S.; Imamoto, Y. *J. Am. Chem. Soc.* **2013**, *135*, 14637–14643.
- (45) Xu, J.; Wu, J.; Zong, C.; Ju, H. X.; Yan, F. *Anal. Chem.* **2013**, *85*, 3374–3379.
- (46) Nagatomo, S.; Nagai, M.; Ogura, T.; Kitagawa, T. *J. Phys. Chem. B* **2013**, *117*, 9343–9353.